NIAC Phase I Final Report

"Antimatter Harvesting in Space"

Research Subaward No. 07605-003-044

Period #1 from September 1, 2005 to March 24, 2006

Dr. Gerald P. Jackson and Elaine T. Marshall
Hbar Technologies, LLC

I. Introduction

NASA has already identified antimatter as the ultimate energy storage medium for exploration at the outer reaches, and outside, of the solar system, a goal well within its mission. Antiprotons naturally produced by the collisions of cosmic rays with dust and solar wind protons have a very low density. However, the solar system is vast. Just as in certain mathematical problems wherein the product of two variables respectively approaching infinity and zero can yield a finite number, the harvesting of antimatter in our solar system can produce finite and significant quantities given a big enough net. The challenge is to envision a revolutionary capture and delivery architecture that generates a sufficient return on investment. Using the fact that the observed peak in the antiproton spectrum is in a kinetic energy band of 1-2 GeV, the underlying revolutionary apparatus envisioned is a set of large concentric spheres that are biased electrostatically at 1 GV to provide deceleration of antiprotons while warding off the solar wind protons. Once decelerated, the residual spread in antiproton kinetic energies is reduced by electron cooling and positron scattering within previously capture antihydrogen. The ultimate goal of this project is to identify and explore the economic, technological, safety, and environmental challenges of an architecture capable of harvesting copious quantities of antimatter in our solar system.

II. Phase I Work Plan

The proposed goals of this project were to computationally evaluate the concept of antimatter harvesting, to develop a workable architecture that captures, cools, and delivers both antiprotons and positrons, and to address the construction issues of these harvesters.

This report is an architectural report describing the launch and deployment of antimatter harvesters; along with the capture, cooling, and antimatter delivery systems required to harvest antimatter in space and return it to Earth, or eventually to other destinations such as refueling depots in a solar system wide transportation network.

In response to excellent suggestions by the proposal reviewers, we have maintained a strong focus on the overall system, and not get too stuck on subsystem details. While constantly looking for experimental opportunities to validate key technologies, in Phase I, and Phase II if awarded, we will reduce our proposed focus on the design of future experiments. Other helpful suggestions from the proposal reviewers were

- Study the interaction of the harvester with a dynamic solar wind model.
- Study the interaction of the harvester with the interplanetary magnetic field.
- Model the interaction of the harvester with solar wind electrons, protons, and ions, including their full energy distributions.
- Model the interaction of the harvester with solar storms from coronal mass ejections.
- Study the effect of high energy galactic cosmic rays on the antiproton distribution.
- Calculate the power requirements for the harvester.
- Improve the references to prior work.
- Develop a suite of simulation tools for predicting the performance of the harvester.

While the calculation of power requirements is still premature given the list of physics concepts that still need to be worked through, it will be an issue addressed toward the end of Phase I. If Phase II is awarded, power requirements will be a key consideration under study.

No show-stoppers have been found in the concept of antimatter harvesting in space. Given the considerable external and internal interest in this project, it is clear that a follow-on Phase II proposal will be submitted to NIAC in 2006. Considerable work has already been performed by students at Embry-Riddle Aeronautical University in Prescott, AZ. It is anticipated that other partners will come on board, potentially from other companies and universities.

III. Overview of Harvesting Architecture

Imagine antimatter harvesting structures orbiting the sun at various azimuthal locations along Earth's orbit. Since the antiproton and positron fluxes are thought to be isotropic and continuous, an efficient capture geometry is spherical in nature. This has been the first geometry studied in this project, though it may become more efficient to transition to cylindrical or toroidal geometries as the research progresses.

Now, imagine a structure capable of harvesting antiprotons at a rate equal to the present terrestrial production rate of 6×10^{14} antiprotons/year, or roughly one nanogram per year. This corresponds to harvesting 16 million antiprotons per second. From figure III.1(a) we know that the incidence rate of antiprotons on a vast spherical surface is 0.02 m^{-2} sec^{-1} sr^{-1} GeV^{-1}. Assuming acceptances of 1 sr and 1 GeV, a surface area of 8×10^{8} m^{2} is required. Such a spherical surface has a radius of 8 km, or 5 miles.
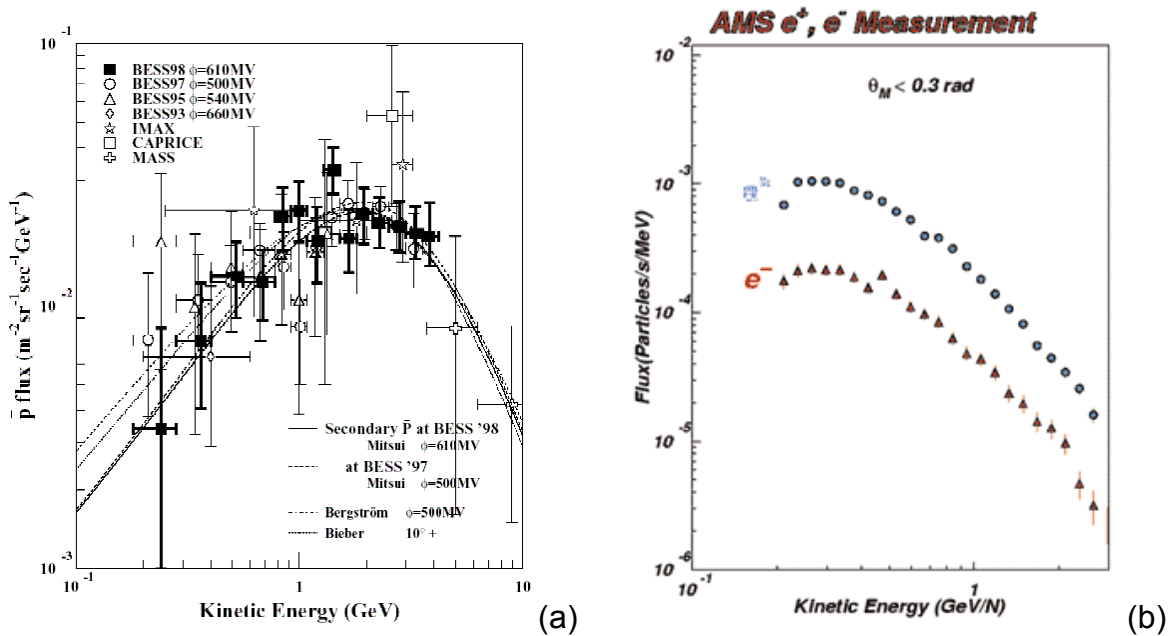
Figure III.1: Compilation of the (a) antiproton and (b) positron flux data.

There is also a large flux of positrons in space. Figure III.1(b) shows the results of one experiment orbiting Earth in the Space Shuttle. Note that the peak of the energy distribution extends out to several 100's of MeV, which is above the kinetic energy region electrostatically shielded by the outer spheres. By reversing the polarity of the harvester spheres, the capture and cooling of positrons Is also possible.

The spherical volume of the solar system out to Saturn is 1.2×10^{37} m^3. In this vast expanse of open space, there are therefore 20 kg (1.2×10^{28}) of antiprotons. Closer to Earth, the toroidal volume between the orbits of Venus and Mars is 4.7×10^{34} m^3. In this "reachable" region of territory, there are 79 g (4.7×10^{25}) of antiprotons at any given time. These antiprotons are constantly replenished and traversing our solar system at close to the speed of light. We are proposing to harvest a renewable resource!

It should be pointed out that there is a great deal of controversy concerning the variation of antiparticle fluxes in the solar system. Near the Earth, the collisions of cosmic rays with the upper reaches of the atmosphere are thought to generate positrons (e+) via pair-production and leptonic decays (see figure III.2). There is another NIAC-funded research project that is looking into the possibility of finding concentrated distributions of positrons and antiprotons in planetary radiation belts. A high priority experiment is to travel the solar system away from Earth to sample the antiparticle density distribution. Students at Embry-Riddle Aeronautical University have started the design of such a science mission.

One of the obvious key issues surrounding this concept of antimatter harvesting is the placement of the collectors. While there is another proposal that is specifically investigating the use of planetary magnetic fields to harvest "concentrated" antiproton populations, it is still necessary and prudent for this proposal to consider the desirability

3

of operating close to planetary atmospheres, in contrast to operations in the interplanetary environment.
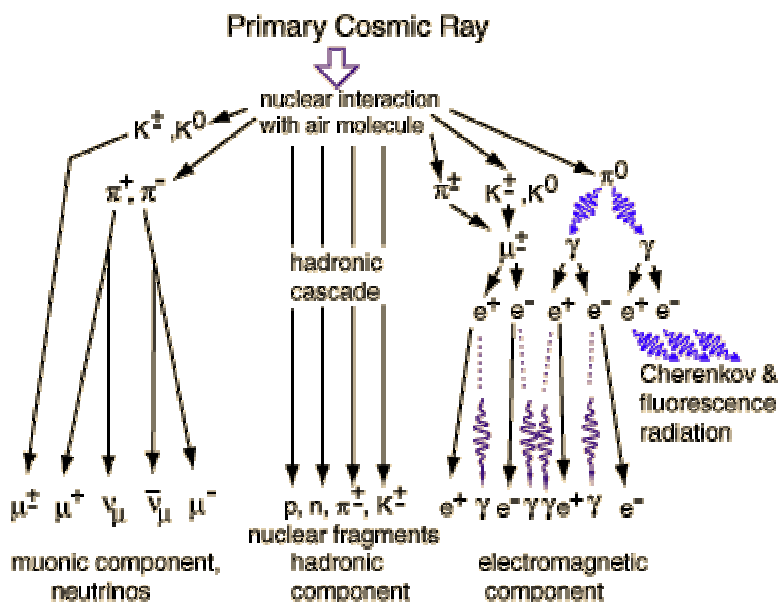

Figure III.2: Positron production mechanism in the upper atmosphere. Though schematically shown as directed downward, many of the processes have a backscattering probability which generate positrons flowing away from the Earth.

Planetary environments have the added complications of magnetic fields and atmospheres. Both of these issues have been studied in extraordinary detail by researchers in France [C. Y. Huang, L. Derome, and M. Buenerd, "Secondary Antiproton Flux Induced by Cosmic Ray Interactions with the Atmosphere", Phys. Rev. D **68**, 053008 (2003)]. Comparing satellite, balloon, and mountain top data with a Monte Carlo simulation they have developed, they have created an accurate model of the antiproton population around the Earth (see figure III.3). This model could clearly be extended to other planets.

One of the interesting conclusions of this paper is that the antiproton flux at the Earth's surface is measurable. While a thousand times lower than the peak flux at 10 km, one could imagine that it might be easier to develop a capture system that has a capture area 1000x larger than a space-borne harvester, laying out on the ground. This corresponds to a planar accumulator that is 30km x 30km, which is quite conceivable

As shown in the paper, the problem is that the absolute flux of cosmic-ray produced antiprotons at an altitude of 38 km is only 15-20% of the antiproton flux found propagating in space. This adds another capture area at sea level increase of 5x to reach the fluxes found in space. On the other hand, by operating at mountain-top elevations of approximately 3 km, an order of magnitude in antiproton flux is gained.
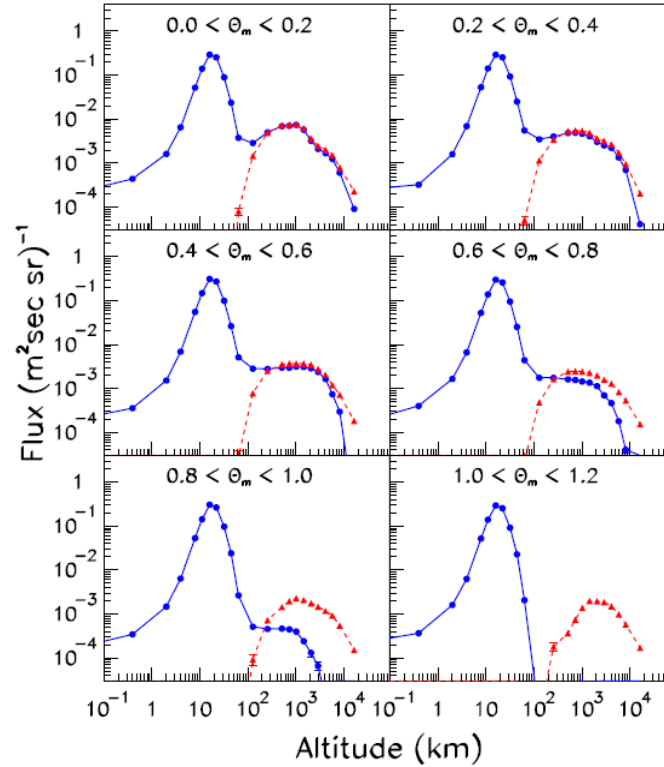
Figure III.3: Reproduced from Huang et. al., altitude dependence of cosmic-ray produced antiproton flux above the Earth in six latitude regions (in radians). The solid (blue) curves are for downward flowing antiprotons, while the dashed (red) curves are for upward propagating particles.

The issue of planetary magnetic fields and their roles on antiproton propagation is also addressed by Huang et. al. As suggested in figure III.4, the effect of multiple entries into the atmosphere during cyclotron oscillations on magnetic field lines is simulated.   In the paper, they study trapped, semi-trapped, and non-trapped antiprotons.

First of all, GeV antiprotons entering a planetary system supporting a magnetic field will be deflected, but not trapped, unless they scatter off atmospheric molecules. This conclusion is as much a result of simulation as a recognition of the applicability of Louiville's theorem to this geometry. Basically, any distribution of particles only exposed to static mean-field forces act as an incompressible fluid in six-dimensional phase space (three spatial and three directional degrees of freedom). In order to compress the spatial distribution of antiprotons, their angular divergences would have to be increased by a corresponding factor. But given that these antiprotons have trajectories in all 4π steradians, no expansion of divergences is possible.

The compression of particle phase space is called cooling. There is electron cooling, which is analogous to mixing a hot gas (the antiprotons) with a cool gas (the electrons), transferring heat to the cool gas. Elastic scattering off air molecules is similar to electron cooling, with the disadvantage that nuclear interactions with the nuclei of those molecules will induce annihilation. There is stochastic cooling, wherein measurement and manipulation of the statistical fluctuations of the population centroid

5

with high frequency electromagnetic fields removes those fluctuations, in turn cooling the distribution. There is also optical cooling, such as optical molasses, wherein sharp absorption resonances for certain photon wavelengths can induce particle deceleration in all three spatial dimension, also causing cooling.
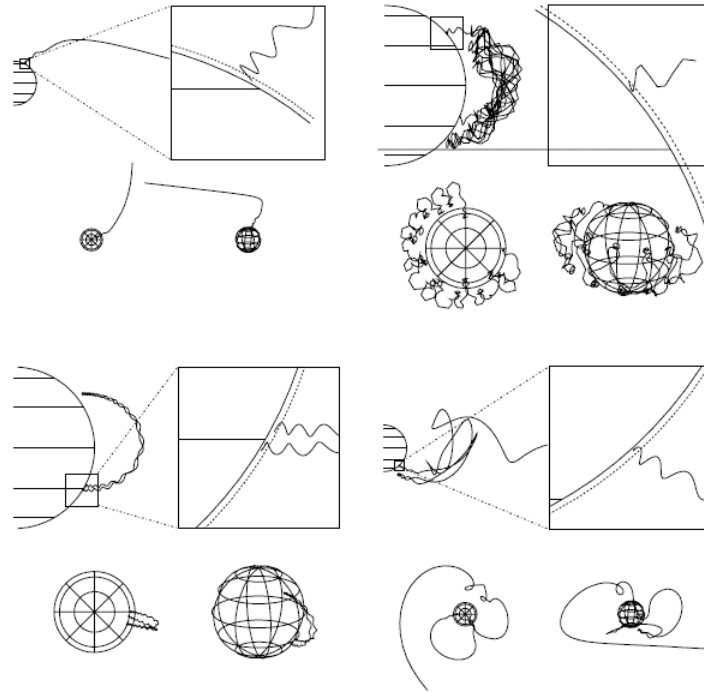

Figure III.4: Reproduced from Huang et. al., calculated antiproton trajectories in the presence of the Earth's magnetic field.

Of these forms of cooling, only molecular scattering is relevant to antiprotons above the Earth's atmosphere. The cross-section for annihilation is so high in comparison with significant elastic scattering that the probability of this form of cooling yielding a significant change in the antiproton population is very low. The paper by Huang et. al. shows that antiprotons created in the atmosphere do not have significant lifetimes.

Specifically, their simulations show no long-lived trapped antiprotons. They see a few quasi-trapped antiprotons which survive a few hundred bounces within the Earth's magnetic field, but this population is statistically insignificant.

Therefore, there is no apparent advantage utilizing planetary magnetic fields. Given the added negative effects of material degradation due to atomic oxygen and orbital debris collisions, we conclude at this moment that operation of antiproton harvesters far from planetary bodies is preferable.

IV. Electrostatic Cage Design

In the proposal, the design of the spherical electrostatic cages were simply shown in figures as dotted lines. One such picture is found in figure IV.1 below. Of course, one cannot build dotted lines. A great deal of time has been spent on understanding the charge distributions, forces, wire configurations, and a host of other issues.

The first detailed calculation was for the gravitational collapse of a simple loop of infinitely flexible wire. Coupled with this work were similar calculations of the centripetal and electrostatic inflation of such a loop. One of the more elegant and simple calculations was to determine the wire voltage required to just offset the gravitational self-collapse force. As shown in figure IV.2, take any two infinitesimal sections of the wire loop and calculate the gravitational force between them. As two point sources of mass, the force between the sections scales as $1/r^2$.
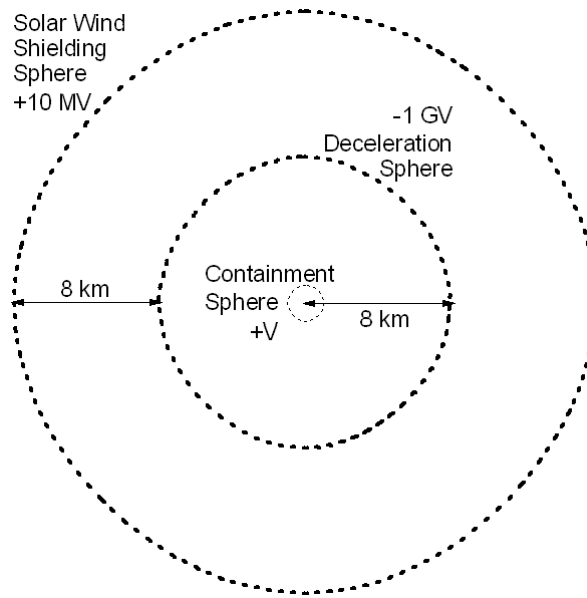

Figure IV.1: Sketch of the spherical geometry presented in the proposal for this project presented to NIAC.
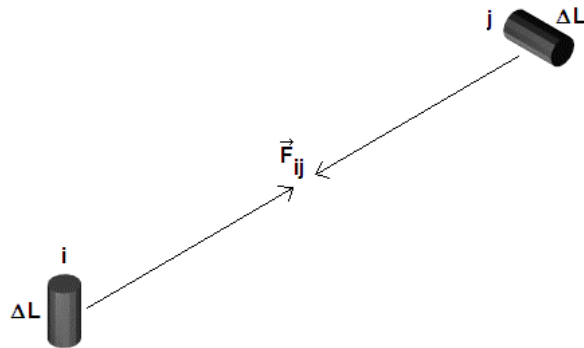

Figure IV.2: Any two infinitesimal line segments on the single loop of wire. The forces from all such segments are integrated to calculate the net force on each segment.

Because the electrostatic force between any two point sources of charge also scales as $1/r^2$, and for a charged loop is repulsive, one can negate the gravitational force between any two line segments, and hence for the entire structure as a whole.

For two line segments of length dl that are a distance D away from each other, the gravitational force F_{ij} can be written as

$$\frac{d^2 F_{ij}}{dl^2} = G_N \frac{\left(\pi a^2 \rho\right)^2}{D^2} \quad , \quad \text{(IV.1)}$$

where a is the wire radius and ρ is the density of the wire material.

The electrostatic wire repulsion between two wire elements can be written as

$$\frac{d^2 F_{ij}}{dl^2} = \frac{1}{4\pi\varepsilon_O} \frac{\lambda^2}{D^2} \quad , \quad \text{(IV.2)}$$

where λ is electrical charge per unit length on the wire. In this situation where the loop radius is MUCH larger than the wire radius a, the relationship between λ and the wire voltage V is well approximated by the equation

$$V = \frac{1}{4\pi\varepsilon_O} \frac{2\lambda}{a} \quad . \quad \text{(IV.3)}$$

Combining equations (IV.2) and (IV.3) to eliminate the line charge density yields the result

$$\frac{d^2 F_{ij}}{dl^2} = 4\pi\varepsilon_O \frac{V^2}{4} \frac{a^2}{D^2} \quad . \quad \text{(IV.4)}$$

By now setting equations (IV.1) and (IV.4) equal to each other, the critical voltage V_c which just counteracts the gravitational collapse of the ring is given by

$$V = \sqrt{\frac{G_N}{4\pi\varepsilon_O}} 2\pi a \rho \quad . \quad \text{(IV.5)}$$

In order to set the scale for the critical voltage, we can insert values into the variables within equation (IV.5). Table (IV.1) contains the results of this exercise. Note that the critical voltage is independent of size of the structure, only depending on the density of the material and the diameter of the wire. Though not quantitatively comparable to the situation of a harvester sphere, qualitatively it is clear that the critical voltage of a wire mesh sphere will be MUCH smaller than the voltages contemplated for the harvester spheres.

While this analytical calculation, and others like it applied to a single loop of wire, are quite instructive for setting the scale of many effects, they are not directly relevant to the fields and forces surrounding a electrically charged spherical wire mesh. We are currently working with ANSYS to develop a numerical multiphysics model of a single loop of wire, and then a sphere, and then a nested group of spheres. Given that the ratio of the wire diameter to the sphere diameter is on the order of 10^9, it is impossible to directly mesh the geometry. We are investigating the use of ten's of thousands of rigid 2-D spars to simulate the wires as a means of numerically simulating the geometry.

Table IV.1: Numerical input values and calculation results for equation (IV.4).

Parameter	Value
Newtonian Gravitational Constant G_N (m^3/kg-s^2)	6.673×10^{-11}
Permittivity of Free Space ε_o (F/m)	8.854×10^{-12}
Wire radius a (m)	1.0×10^{-5}
Density of titanium wire ρ (kg/m^3)	4507
Critical Voltage V_c (V)	0.22

Over the project duration covered by this report, two designs of spherical wire meshes have been studied. The first was a classic mesh of wires composed of wires at regular intervals of longitude (longitude wires) and wires at regular intervals along the z-axis (latitude wires). This design is shown in figure IV.3(a). The reason for using regular intervals along the z-axis, instead of regular intervals of latitude (such as every 10°) is that one obtains a mesh in which every region between wires has equal area. Assuming that one wants to keep the charge density along each wire relatively uniform, this is the desired solution.

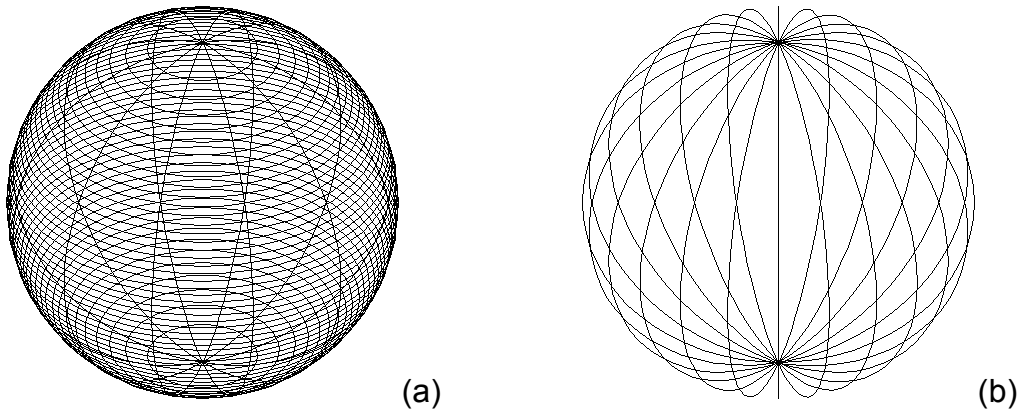(a)   (b)

Figure IV.3: (a) Classic wire mesh sphere in which wires at equal intervals of longitudinal angle (longitude wires) and wires at equal intervals along the z-axis (latitude wires) are used to construct the spherical structure. (b) Wire mesh sphere composed solely of longitude wires.

For reasons described in a later section discussing sphere deployment, an alternative approach is to create a spherical mesh composed solely of longitude wires. It was realized early in the course of this project that wires at the same voltage will repel each other, making latitude wires unnecessary. This geometry is shown in figure IV.3(b). Most of the effort in the next months will be centered on this alternate spherical geometry.

Since the first report, we have worked extensively with engineers at ANSYS to set up this problem within their multiphysics simulations code. Because of the dynamic

range of spatial scales, dealing simultaneously with micron wires and kilometer loops, two-dimension structural elements were chosen. These elements hold charge, support electrical currents, can hold heat, can radiate heat, and can elongate elastically.

The only geometry within the scope of Phase I we will be able to study is that of a single loop of wire. During Phase II the entire harvester geometry will be simulated. Below we present the results of preliminary single loop calculations of the static response to electrostatic forces.
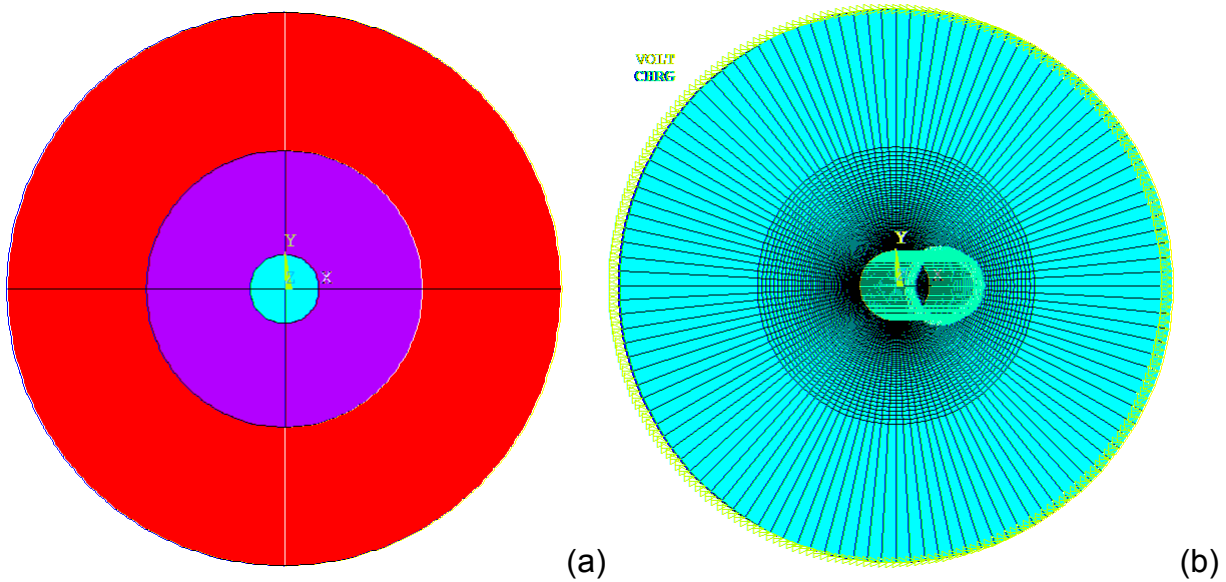

(a)   (b)

Figure IV.4: Setup of the single-wire ANSYS calculation. In (a) the wire (inner region), electrostatic calculation area (purple region), and the infinite potential normalization (red region) are shown. In (b) the non-zero charge and voltage on the wire is shown in 3D.

Figure IV.4 shows the geometry of the single loop of electrostatically charged wire in free space. In figure IV.4.a, there are three shaded regions, with the inner region the inside of the wire loop itself, the middle region the area of grided electrostatic calculation, and the outer region the interval used by ANSYS to calculated electrostatic fields in an open (infinite) geometry.

In figure IV.4.b, the 3D extension of the mesh shows the charge of the wire and lack of electrostatic charges anywhere else in the problem. Also, the green triangles at the edge of the open geometry calculation shows the assumed lack of electrostatic potential and infinite distance from the loop.

Figure IV.5 shows the electrostatic potential and radial electric fields. The color coding in figure IV.5.a indicates the electrostatic potential in the plane of the single loop. While the potential is defined as zero an infinite distance from the loop, note that the inside of the loop is essentially at constant potential. As seen in figure IV.5.b, the radial electric field is zero inside the loop is close to zero, explaining the constant electrostatic potential in that region. A few diameters from the wire the potential drops as the inverse of the distance, while the radial electric field drops as $1/r^2$.
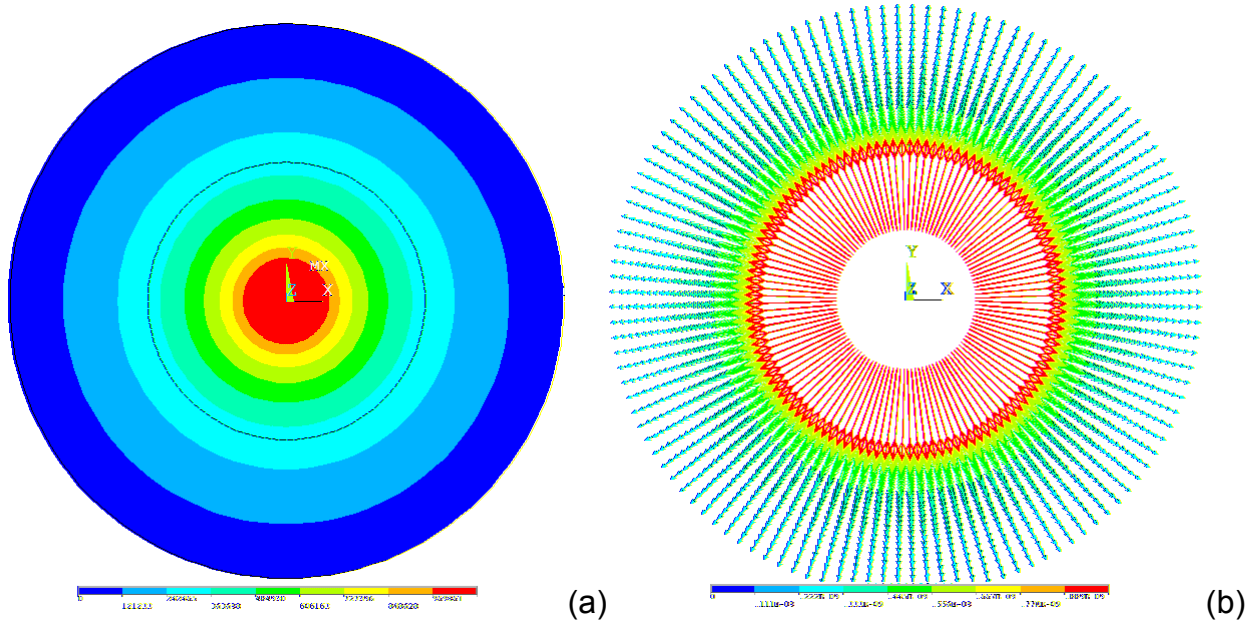
(a)

(b)

Figure IV.5: Electrostatic potential (a) and electric field (b) of the space around the wire. As expected, the potential inside the loop is maximal, the electric field is zero inside the loop is zero, and the electric field is purely radial.
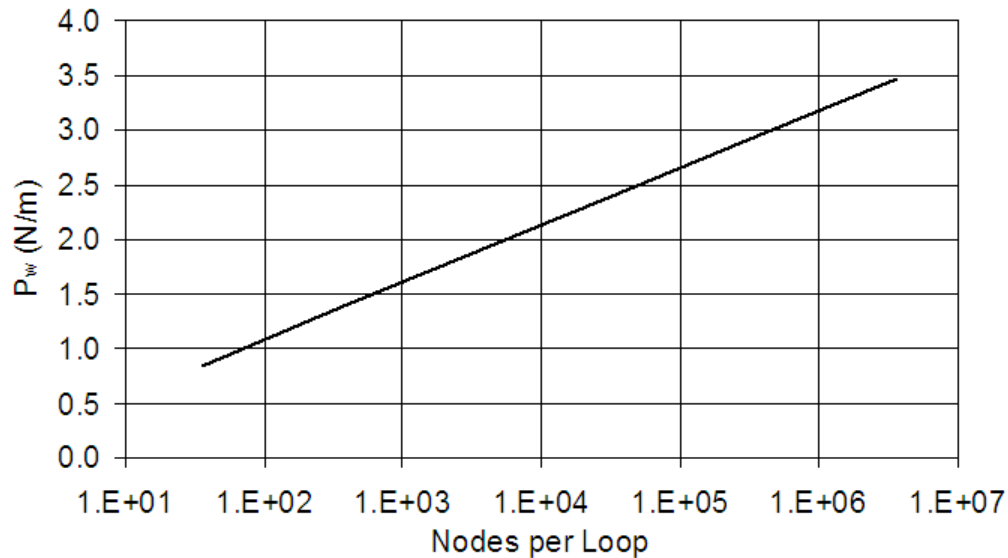

Figure IV.6: Calculated radial pressure on the loop of wire, for a fixed total charge on the wire, as a function of the number of discrete charges in the calculation.

The radial electric field at the wire times the charge per unit length on the wire results in a radial pressure on the wire (pressure in this case is force per unit length, not per unit area). In order to calculate the tension T_w on the wire, one spatial component of this pressure P_w is integrated over one quarter of the circumference

11

$$T = \int_{0}^{\pi/2} P_W \, R \sin\theta \, d\theta \ = \ R \, P_W \qquad\qquad . \qquad\qquad (IV.1)$$

In the ANSYS simulation, and a home-grown Hbar Technologies, LLC simulation, a continuous wire with a continuous charge distribution on it is replaced with a finite number of discrete charges. Figure IV.6 shows the sensitivity of the resultant calculated pressure as a function of the number of discrete charges around the wire, keeping the total charge on the wire constant.
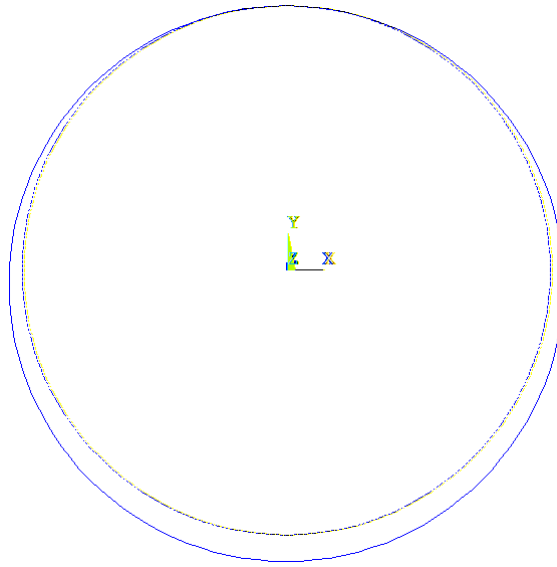

Figure IV.7: ANSYS calculation of the stretching of the wire under the electrostatic forces induced by the uniform excess charge on the wire. The top of the loop was held fixed, so the stretching acted downward and outward. This plot is exaggerated, where the difference in diameter is actually 4 cm.

In ANSYS Multiphysics™, the tension calculated from this pressure (using equation IV.1) is applied to the elastic spars between each discrete charge to calculate the stretching of the wire due to this tension. Figure IV.7 shows one such calculation, wherein the discrete charge at the top of the wire loop is held fixed and the other charges are allowed to move. Note that figure IV.7 is not to scale. For a 10 km diameter loop, the increase in diameter due to this tension is 4 cm.

V. Initial Cooling of the Antiparticles

A great deal of progress has been made on understanding the physics involved in the initial cooling of the antiparticles which make it inside the deceleration sphere (see figure IV.1). In the proposal, the concept was to load the volume inside the deceleration sphere with electrons. It was proposed to use collisions with electrons over distances of

kilometers to provide the required electron cooling of the antiproton kinetic energy distribution. For example, collisions off electrons in hydrogen gas are responsible for the majority of kinetic energy loss suffered by more massive particles. At standard temperature and pressure, hydrogen gas has a density of 0.072 g/cm^3 and an initial stopping power of 0.37 MeV/cm. Under these conditions, a 1 GeV antiproton would stop in 22 m. The density of electrons under these conditions is 5x10^{22} electrons/cm^3. In order to obtain a stopping power of 1 GeV in 8 km, the minimum electron density is 1.4x10^{20} electrons/cm^3 or an equivalent pressure of 0.0028 atm (at 0°C). Hydrogen gas could be used, but the protons would scatter and annihilate the antiprotons, hence reducing the harvesting efficiency.

There is a big problem with the idea of a pure electron cloud inside the deceleration sphere. Aside from the obvious issue of how to store these electrons, the voltage developed at the surface of this cloud is truly astronomical!

Assume a uniform spherical spatial distribution for the electron cloud. Since we know that the radial electric field E$_r$ inside this sphere can be written as

$$E_r = \frac{1}{4\pi\varepsilon_o}\frac{Q_{enclosed}}{R^2} \qquad , \qquad (V.1)$$

where the charge enclosed by the sphere of radius R, given a uniform spatial distribution of number density ρ_q, is

$$Q_{enclosed} = \frac{4}{3}\pi R^3 e\rho_q \qquad , \qquad (V.2)$$

the radial dependence of this electric field inside the cloud is

$$E_r = \frac{e\rho_q}{3\varepsilon_o}R \qquad . \qquad (V.3)$$

The voltage inside, and on the outer surface of, the cloud is given by the radial integral of the radial electric field in equation (V.3). Performing this integral yields

$$V = \frac{e\rho_q}{6\varepsilon_o}R^2 \qquad . \qquad (V.4)$$

For the case of an electron cloud inside of the deceleration sphere, assuming that all spheres are missing for the purposes of this calculation, the self-fields of the electron cloud are calculated in table V.1. With respect to a point an infinite distance away from the cloud, the desired surface voltage would have been 1 GV. This electron cloud distribution has a surface voltage which is 14 orders of magnitude larger!

The solution to this problem is neutralization of the electron cloud. Two possibilities have been considered so far. The first, as mentioned in the proposal, is to use hydrogen atoms. An offshoot of this approach is to use fully ionized nuclei of very high-Z, thereby reducing the number density of these nuclei proportional to Z. At this time this is considered to be the most fruitful approach.

Table V.1: Numerical input values and calculation results for equation (V.4).

Parameter	Value
Spatially uniform electron cloud density ρ_q (m^{-3})	1.4×10^{26}
Permittivity of Free Space ε_o (F/m)	8.854×10^{-12}
Charge of the electron e (C)	1.602×10^{-19}
Radius of the cloud R (m)	8000
Radial electric field at the electron cloud surface E_r (V/m)	7×10^{21}
Electron cloud surface voltage V (V)	3×10^{25}

The second approach that was investigated involved the neutralization of the electron cloud with an overlapping positron cloud. At sufficiently high temperature, the electrons and positrons stay well mixed and do not annihilate against each other too quickly.   Figure V.1 show the annihilation cross section σ between electrons and positrons as a function of relative kinetic energy.   The average probability P_1 of a positron annihilating while passing once through a spatially uniform cloud of electrons of radius R and density ρ_q can be approximated by

$$P_1 = \sigma R \rho_q \qquad . \qquad (V.5)$$

If the desired probability P_1 is 10^{-6}, then for the parameters in table V.1 the cross section must be equal to 9×10^{-37} m^2. As can be seen from figure V.1, the desired probability cannot be attained with the density of electrons in table V.1, even for positrons with a kinetic energy of 1GeV. To reach such probabilities, the electron density must be reduced by 5 orders of magnitude.
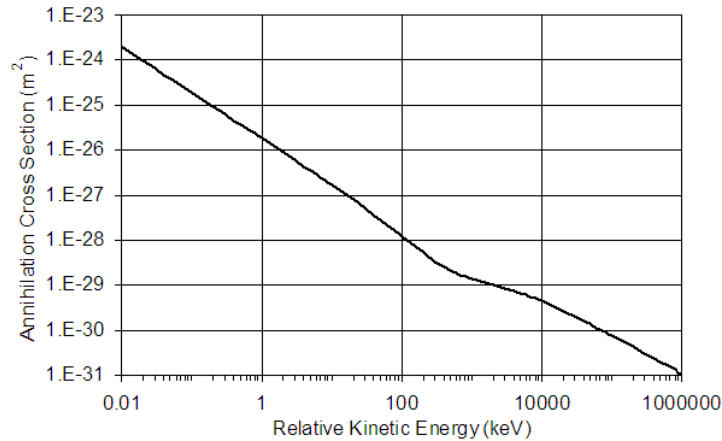

Figure V.1: Annihilation cross-section between a stationary electron and a moving positron of a given kinetic energy T. Note that the cross section decreases with a 1/T power law (except for the dip at 1 MeV).

More progress has been made on understanding the physics involved in the initial cooling of the antiparticles which make it inside the deceleration sphere (see figure IV.1). In the last report, it was pointed out that under STP conditions hydrogen gas has

a density of 0.072 g/cm^3 and an initial stopping power of 0.37 MeV/cm, stopping a 1 GeV antiproton in 22 m. In order to obtain a stopping power of 1 GeV in 8 km, a hydrogen pressure of 0.0028 atm (at 0°C) is required. Hydrogen gas could be used in the harvester, but the protons would scatter and annihilate the antiprotons, hence reducing the harvesting efficiency.

On the other hand, positively charged ions of hydrogen (a single antiproton orbited by two positrons) would be trapped and provide cooling without annihilations. Because there are two positrons per antiproton, the required density for needed level of dE/dx is half of the required neutral hydrogen density. Of course, the problem with this idea is that the mass of antihydrogen inside the deceleration sphere is 2.7x10^{17} cm^3 x 0.072 g/cm^3 x 0.0028 x ½ = 27x10^9 kg! If this amount of antimatter were available, we would not need the harvester!!!

These issues of annihilation and scattering are described in terms of energy-dependent cross sections. Because much of this data is described in terms of the momentum of an incoming particle with respect to stationary target particles, figure V.1 contains a calibration plot between incoming momentum and kinetic energy for both antiprotons and protons. Note that a kinetic energy of 1 GeV corresponds to a momentum of 1.7 GeV/c.
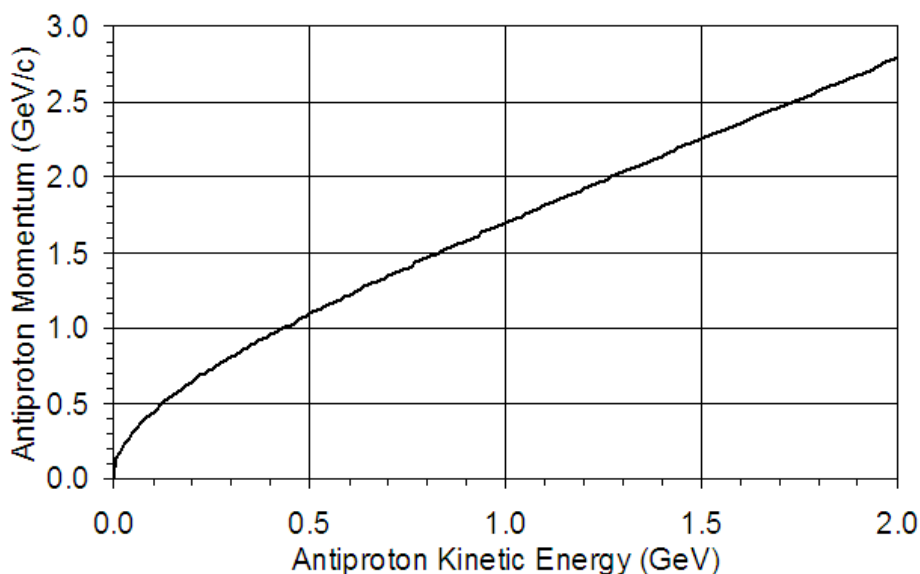

Figure V.1: Comparison between kinetic energy and momentum for a proton or antiproton which is incident on target particles.

Figure V.2 shows the accumulated data on the elastic and total cross sections between an incident proton on target protons (or an incident antiproton on target antiprotons). Elastic collisions are those where the two particles that entered the collision come out of the collision, though not always the same two particles! The total cross section describes the effective area of the target particles wherein all permutations of collisions are included, such as annihilation or fragmentation into other elementary particles. Cross sections are in units of barns, as in hitting the broad side of

a barn. One barn is equal to an area of 10^{-28} m^2. The units in both figures V.2 and V.3 are in millibarns.
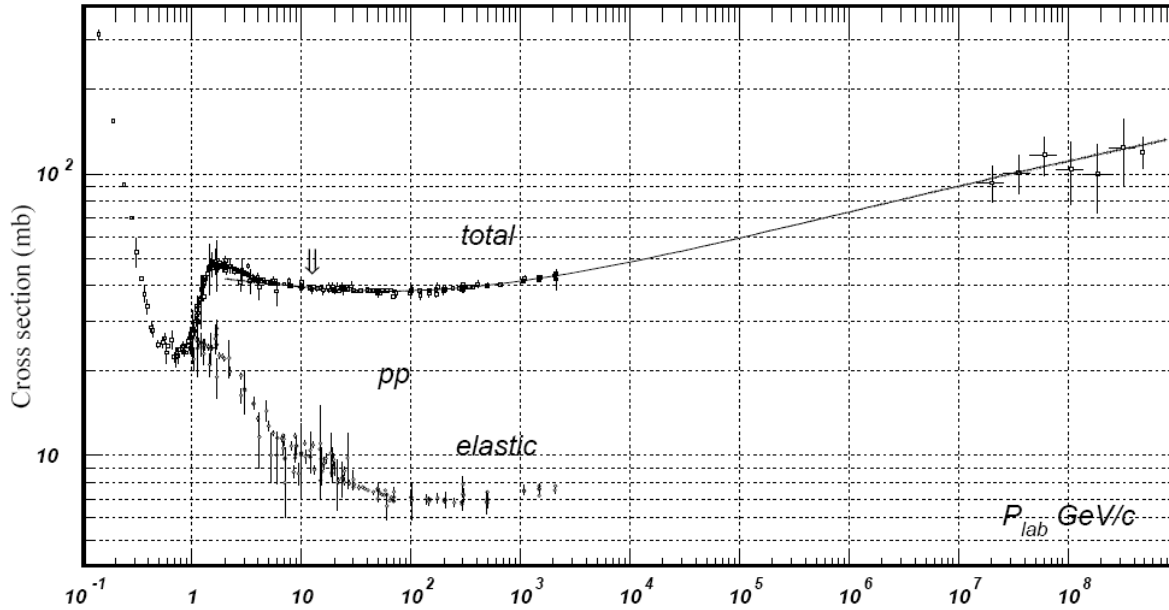

Figure V.2: Cross sections for incident protons on stationary protons, or incident antiprotons on stationary antiprotons.
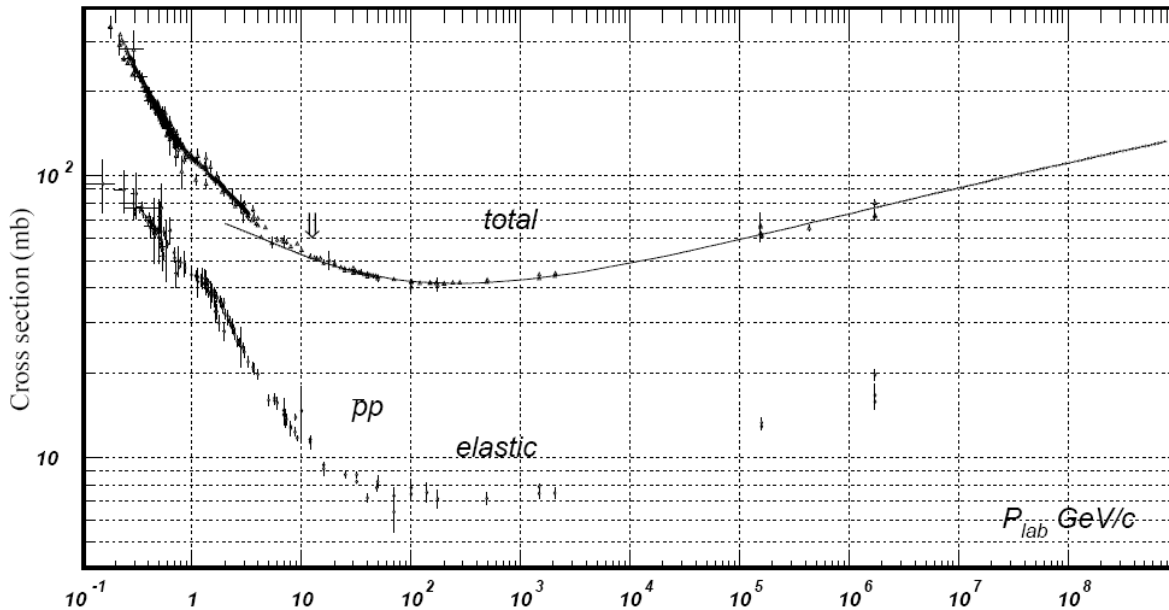

Figure V.3: Cross sections for incident protons on stationary antiprotons, or incident antiprotons on stationary protons.

To correlate the cross sections in figure V.2 and V.3 with annihilations, it is necessary to multiply the cross sections by the number density of target particles over the length of interest to yield an interaction probability. For example, for the case of

hydrogen at 0.0028 atmospheres over a distance of 0.1 km, the probability of interaction for a 1 millibarn cross section is given by 1.4×10^{20} protons/cm^3 x 100,000 cm x 10^{-25} cm^2 = 0.14. This means that over the 100 m of travel in this density, 14% of the incident particles would have suffered the given type of interaction represented by the cross section. In the case of antiprotons colliding with antiprotons, most interactions would be elastic (the inelastic cross section goes to zero near a kinetic energy of 0.3 GeV), which is why using antihydrogen to cool incident antiprotons is so desirable.

On the other hand, collisions between protons and antiprotons are always dominated by the total cross section, with roughly 1/3 or all interaction being elastic and 2/3 representing fragmentation or annihilation (called inelastic collisions). It are these inelastic collisions that make the use of hydrogen as a source of antiproton cooling so problematic. As seen in figure V.3, the antiprotons in the 0-1 GeV kinetic energy acceptance of the harvester have an inelastic cross section between 100 millibarns and higher. In the above numerical example, 100 millibarns yields a 14% annihilation probability for every meter of travel. Clearly, after a few meters, almost all the antiprotons would be gone.

Therefore, positrons and electrons in some form of two-stream plasma or stable positronium are still the optimum medium for initial antiproton cooling. In the last report, it was shown that two-stream plasmas must be very high temperature to prevent electron-positron annihilations. Another possibility, which we have recently begun to work on, is forming alternating radial spherical halos of electrons and positrons to counteract the large space charge forces found in non-neutral plasmas.

VI. Interaction with Interplanetary Neutral Particles

In the beginning weeks of the project, one of the issues that became a big issue was the effect of neutral particles traveling into the harvester. There are three classes of neutral particles. The first class is dust with an excess charge insufficient to deflect or reverse the trajectory of the particle. The second class is neutral atoms. The third class is neutrons.

According to the Backman Report, titled "Extrasolar Zodiacal Emission - NASA Study Panel Report": "The sources of [interplanetary dust particles] IDP include at least: asteroid collisions, comet activity and collisions in the inner solar system, comet collisions in the Kuiper Belt (KB), and ISM grains. The main physical processes affecting IDP are: expulsion by radiation pressure, inward Poynting-Robertson radiation drag, solar wind pressure (including significant electromagnetic effects), sublimation, mutual collisions, and gravitational influence of planets.

No rigorous accounting has been made of the relative strengths of the grain sources, nor of the effects of the various destruction and dynamical processes on the equilibrium spatial distribution of the dust. Difficulties arise not simply because of complex cloud structure but also from problems in comparing multi-wavelength data sets which do not measure precisely the same lines-of-sight simultaneously and are often subject to large calibration error. Very different models of the spatial distribution of the material have produced acceptable fits to visual and IR data (e.g. Giese and Kniessel 1989). Much work remains to be done combining observational data with a priori models of the spatial distribution based on dynamical evolution of the grains."

Given this situation, it is very difficult to address the concern of dust particles entering the harvester. This is clearly an area where more work is necessary. One potential approach is to calculate the charge-to-mass ratio of dust particles required to deflect the dust particles, given a velocity distribution that is similar to that for asteroids and comets which pass through the Earth's orbital radius.

The second class is neutron atoms. The dominant gas is hydrogen, which far from the sun is found in neutral atom form. Closer to the sun, the solar ultraviolet photons ionize the hydrogen gas. The boundary between these to regions is called the Stromgren radius. Because recombinations compete with the ionization process, gas pressure and temperature as well as UV photon density all play a role in the calculation of the Stromgren radius. As shown in figure VI.1, the Stromgren radius may have changed dramatically over the last few billion years as the solar system has traversed highly varying regions of galactic material densities. More work is required to calculate this radius for helium and other gases, and to understand the neutral atom density distribution in the radial region from the Sun near the orbit of the Earth.
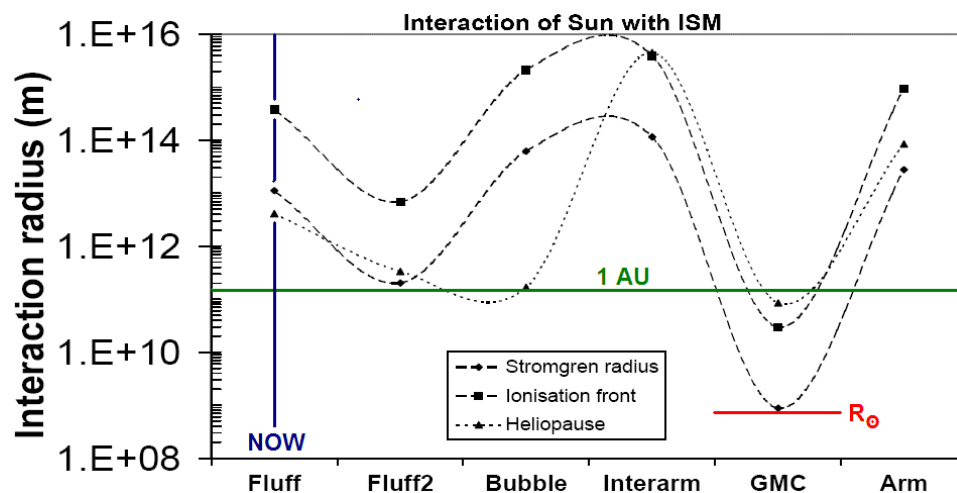

Figure VI.1: Hypothesized evolution of the heliopause, ionization front, and Stromgren radius going backward in time from "Fluff" to "Arm". Note that while there have may have been a time when the Stromgren radius was actually at the solar suface, but is now outside of the heliopause.

In researching the third class of neutral particles, it is important to remember that the lifetime of free neutrons is 886.7 sec. Assuming production via cosmic collisions with the solar wind/dust/atmospheres and direct solar flare production, typical kinetic energies of 100 MeV to 1 GeV correspond to neutron velocities of 0.43c to 0.88c, respectively. These velocities correspond to free neutron ranges of 1.1×10^{11} to 2.3×10^{11} m, or approximately 1 AU. Because the probability of neutron production from cosmic ray interactions is higher than antiproton production, and because of the large periodic flux of neutrons from solar flares, the neutron flux into the harvester will be much larger than the antiproton flux. We did not have enough time during Phase I to calculate neutron moderation rates and annihilation probabilities.

VII. Interaction with Static Solar Wind

In the proposal for this study there was already considerable mention of harvester interaction with the solar wind. One criticism by a reviewer was that the simulation of particles incident on the harvester did not include a wider variety of particle species, energy spread, and particle trajectory divergence.

The first response is no kidding, given that the reviewer was reading a proposal to do the research, not a finished product after the research had taken place. Second, the physics of kinetic energy vs. potential energy pretty well dictates that for a given electrical potential, no charged particles will "get over the hill". The details of trajectories and species, while of academic interest, do not affect the anticipated performance of the electrostatic barriers against incoming external charged particles.

That said, there are literally dozens of issues that do need to be resolved given a static flux of charged particles streaming toward the harvester. The primary issues are the equilibrium shape of a wire mesh that is spherical in the absence of such a flux, the reaction of the harvester structure to the thrust induced by deflecting the trajectories of those charged particles, and the steady-state power required to maintain the sphere voltages.

The power issues are addressed later in this report. The shape and center-of-mass motion of the harvester under the influence of a static solar wind are being addressed theoretically and via computer simulations. At present the theoretical calculations are centered on the shape and trajectory of a single loop of wire wherein the solar wind flux is attacking the loop from the side. This geometry is also being simulated with a multiphysics computer program being written by Hbar Technologies, which in turn is being benchmarked by engineers at ANSYS using ANSYS.

The ANSYS team is interested in this problem since it represents a geometry wherein the ratio of the loop diameter to the wire diameter is nine orders of magnitude, making direct meshing of the geometry impossible on computers available today. But we are confident that there is a loop diameter at which the dynamic range of distance scales is sufficiently constrained to allow comparisons between the Hbar Technologies code and ANSYS.

Once this benchmarking is complete, progressively more detailed geometries will be attempted until a validated simulation of the solar wind response of a harvester is achieved. While full harvester modeling was not accomplished in Phase I, it is clear to us that this goal can be met during Phase II if awarded.

VIII. Interaction with Dynamic Solar Wind

As in the case of the static solar wind calculations, the understanding of harvester response to solar wind transients is being addressed with both theoretically and computer simulations. Similar to the static case, at present a single loop of wire is being studied to understand normal mode oscillations and shape stability.

It is expected that both the Hbar Technologies numerical model and the ANSYS simulation of the harvester, once validated for static solar wind effects, will be applicable to the study of transient responses. In the mean time, some straightforward statements can be made on the subject given data currently accessible.

The variations in the solar wind can be tied to solar flare intensity, which varies over a very wide range. At solar maximum, every 11 years, the flux of solar wind protons is maximum. These protons have an energy range between 10 MeV and 1 GeV. During a major flare, proton fluences of up to 2×10^{10} p/cm^2 have been observed.
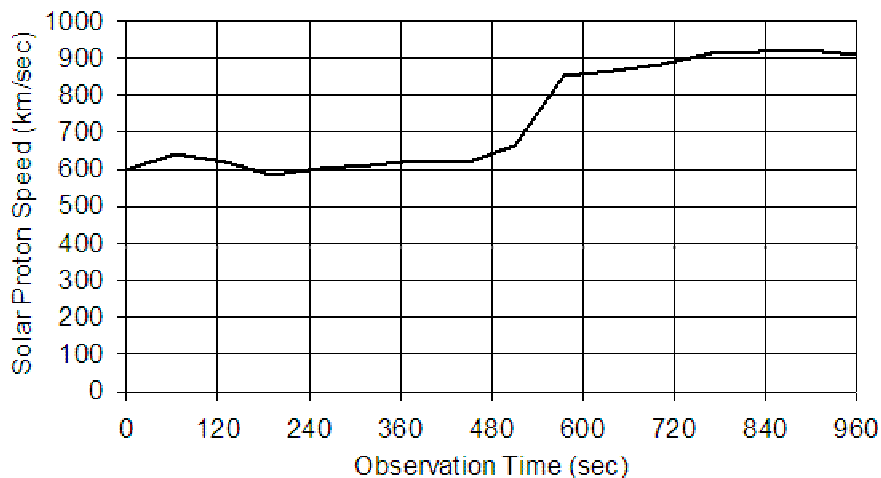

Figure VIII.1: Plot of an observed jump in solar proton speed due to a flare [ACE SWEPAM data]. Note that the majority of the rise took place in a single 64 sec measurement.

The change in solar proton energy can occur in a matter of tens of seconds. One solution is to always run the overall positive potential of the harvester at the outer sphere at +1 GV. This ensures that no high energy protons from solar activity will penetrate the harvester.

Another solution is to give the electron ejection accelerator, responsible for charging the overall structure, sufficient electron current capacity (sending the electrons into space at the necessary electrostatic escape velocity) to increase the voltage from zero to 1 GV in a matter of a minute or so. At a radius of 16km and a surface voltage of 1 GV, the required net charge on the harvester is approximately 1000 Coulombs. In order to achieve this level of charging in 100 seconds, 10 Amperes of charging current is required. Assuming 10 linear accelerators spaced around the structure, this corresponds to a peak electron beam power of 1 GW per accelerator. This corresponds to a stored energy of 100 GJ. Given that the cost of accelerators scale with peak power, it seems that the most efficient solution is run the harvester with a steady-state surface voltage of 1 GV.

IX. Interaction with the Interplanetary Magnetic Field

One of the issue not mentioned in the proposal was the eddy currents set up in the sphere wires due to changing magnetic flux through each loop. In principle, a simple fix is to use an insulator at the top and bottom of the sphere where the longitude wires meet. The problem is that if the voltage drop between wires is too large, the space plasma surrounding this junction could transmit the electrical current. If the impedance

of this alternative path is sufficiently large, then the current in the wires is too small to cause melting or excessive elongation.

The voltage at a break in a single loop (a pair of longitude wires) is proportional to the time rate of change of the magnetic flux lines through the loop. Most of the power spectrum of the Sun's magnetic field is measured in the milliHertz scale. The average magnitude of the Sun's magnetic field at the orbit of the Earth is approximately 10^{-9} Tesla. Assuming a loop radius of 16 km, corresponding to an area of 10^9 m^2, the maximum average flux through the loop is 1 Weber. Assuming either a 100 sec rotation rate of the wire loop or a 10 mHz field oscillation frequency, one expects a voltage at the break in the loop of approximately 10 mV.

Given the small cross-sectional area of the wire and circumference of roughly 100 km, the loop resistance alone should be so high as to make the resultant current in a completed loop completely negligible. To perform a worst-case estimate, assume that the wire is copper. Even at the large wire diameter of 1mm (again, a worst case estimate that is not even feasible for launch mass reasons), the copper resistivity of 1.7 $\mu\Omega$-cm times the circumference of 10^7 cm divided by the cross-sectional area of 0.0314 cm^2 yields a loop resistance of 541 Ω. The current in the loop is therefore 18 μA, and the total power generated over the entire 100 km length is 0.18 μW.

The next step is to develop a quantitative model that includes the forces cause by the interaction of this small eddy current and the interplanetary magnetic field. Because all of the other forces on the spherical mesh structures are so small, there is a chance that this interaction might have a measurable effect.

X. Interaction with Incident Electrons

As mentioned earlier, the interaction of the harvester with the solar wind needs further attention, with implications for the power budget of the harvester. As shown in the proposal, an overall positive charge on the harvester structure will deflect the solar wind protons and ions before they come within the radial range of the structure itself.
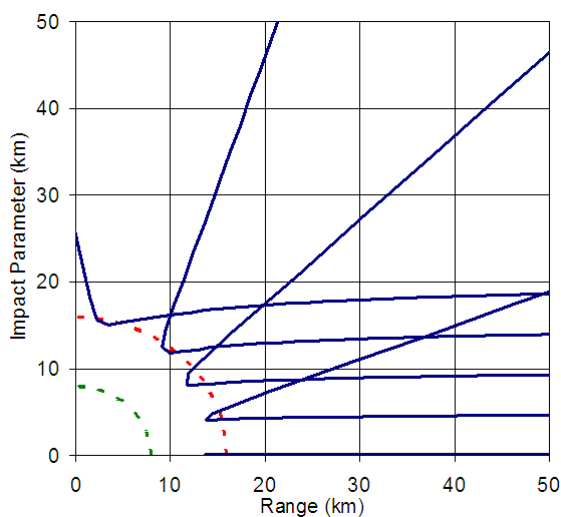

Figure X.1: Select solar wind electron trajectories in the neighborhood of the outer harvester sphere.
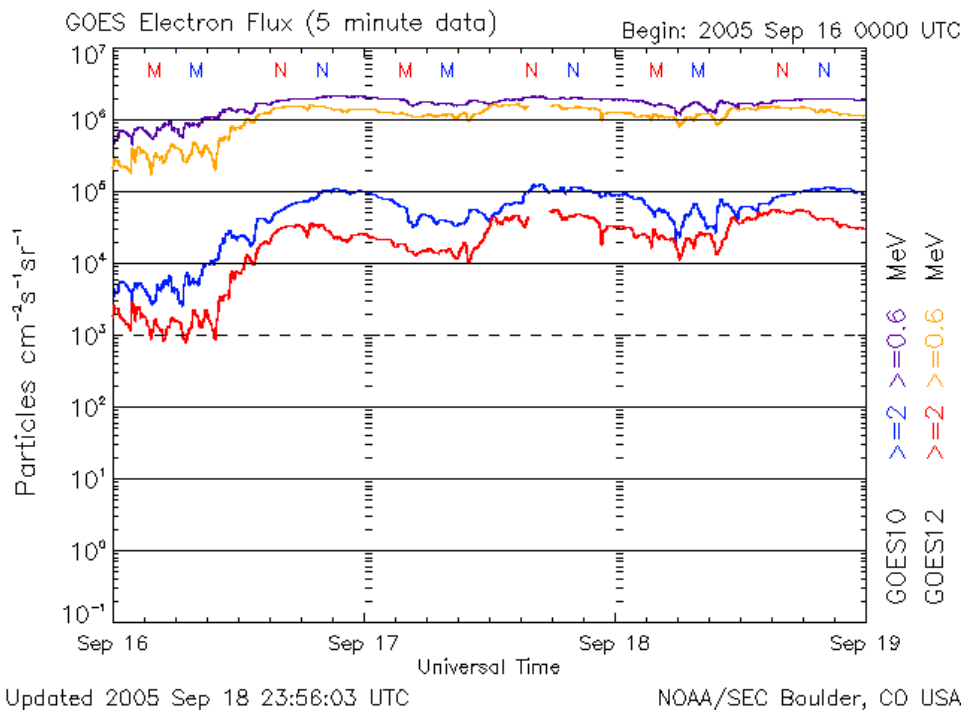
21

Figure X.2: Electron flux data from NOAA for 9/16-18/2005.

On the other hand, figure X.1 shows that the radial electric field between the outer and deceleration spheres (see figure IV.1) will deflect the solar wind electrons once the electrons have passed through the outer sphere structure. Assuming a 1 mil diameter tungsten wire mesh with a 10 m pitch, the probability for collision with the outer sphere wires is approximately 10^{-5}.

Figure X.2 contains a plot from www.sec.noaa.gov/ftpdir/plots/electron/ that shows measured electron flux in Earth orbit. Assuming an electron flux of 10^{10} electrons/m^2-s at the harvester, and an outer sphere cross-sectional area of 8×10^8 m^2, one obtains an incident current of 1.3 A. Multiplying by the probability of collision, the current that would naively have to be accelerated into space to counteract this neutralization flux is 13 μA. Assuming a electron accelerator is used to eject electrons into space to obtain the net charge of the harvester, and under worst-case conditions this accelerator operates at 1 GeV with 10% power efficiency, the power required to maintain the harvester charge is 130 kW.

One possible way to mitigate this de-charging effect is to operate the harvester such that the net attractive radial electric field outside of the outer sphere is set to the point where the wire material has a maximum secondary electron coefficient at the median incident electron energy near the outer sphere. It is well known in the accelerator community that aluminum, copper, and stainless steel have regions in which the secondary electron coefficient under surface electron bombardment is greater than unity, resulting in amplification. As an example, figure X.3 contains data for many materials for a fixed electron incident kinetic energy of 70 MeV. This is in fact the principle behind image intensifiers and photomultiplier tubes. It may be possible to bias the net potential of the harvester to reduce the power requirements for net voltage

maintenance by orders of magnitude. This issue will be pursued further during Phase II if awarded.
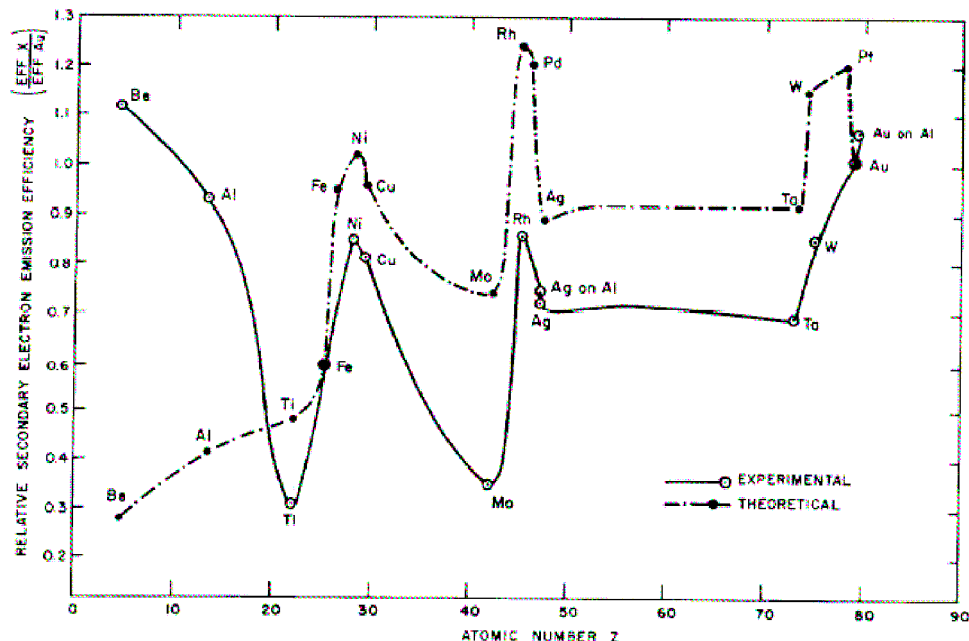

Figure X.3: Secondary electron emission coefficients for incident 70 MeV electrons on thin targets. Note that there are many metals with coefficients greater than unity.

XI. Interaction with Galactic Cosmic Rays

To first order, there is nothing that can be done about high energy galactic cosmic rays traversing the harvesters. On the other hand, the entire cosmic ray spectrum extends down below 1 GeV, where the biasing of the electric potential outside of the outer sphere does deflect protons and heavier ions. Figure XI.1 contains a plot of the energy spectra, as well as the time variability of the proton flux with solar cycle phase.

Though a numerical integration has not yet been done (or found), it is apparent that the majority of cosmic ray ions will not be deflected by the harvester outer sphere. Once ions are inside the radius of the outer sphere, they are accelerated inward to the deceleration sphere with a minimum kinetic energy of 1 GeV. At these energies the ions have a very small cross-section for annihilation with antiprotons. The outstanding issue is that the same dE/dx interactions which initially cool the incident antiprotons will also cool the incoming ions.

The high energy tail of the distribution in figure XI.1 above a few GeV will only make a single pass through the harvester. The low energy region below 1 GeV will not make it into the harvester at all. The next step, hopefully during Phase II, is to understand the fate of those ions between these extremes that might become cooled and trapped.
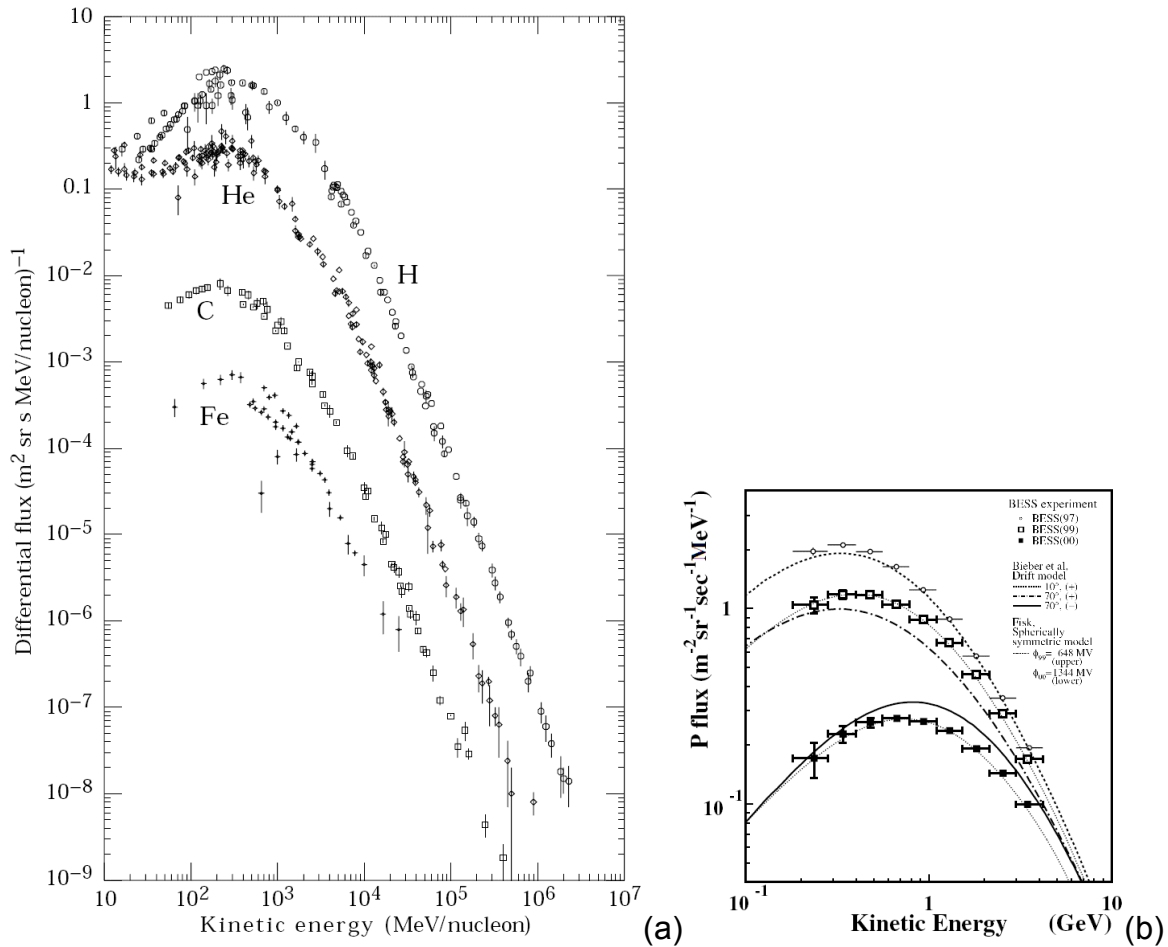
Figure XI.1: Cosmic ray flux for multiple ion species (a) and for hydrogen at various times (b) in the solar cycle. Note that the two plots have different kinetic energy units on the horizontal axis.

XII. Power Requirements

One source of power consumption has already been discussed in section X discussing the harvester interaction with external electrons. Another potential source of power consumption is the generation and storage of particles used to initially cool the incoming antiprotons via dE/dx. Yet a third area of power consumption is the actual bottle at the center of the harvester that holds the harvested antiprotons.

Work has been started on the second source of power consumption. No work has yet been performed to study the third source, but will be one of the primary issues to be studied during Phase II.

XIII. Deployment of the Harvester

It was initially envisioned that each sphere of the harvester structure would be composed of latitude and longitude wires as sketched in figure IV.3(a). A design study led by senior Jeff Turpin at the Embry-Riddle Aeronautical University in Prescott, AZ

had difficulty imagining how to package this configuration is a small enough volume to fit within the cowling of a Delta rocket.

After a conference call with the students, it was realized that the electrostatic forces of the charged sphere will keep longitude wires equally spaced without the need for support from latitude wires. Figure XIII.1 is a classic example of this effect, called a Leyden jar.
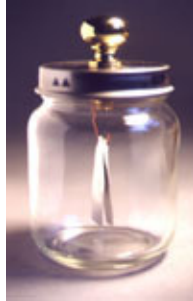

Figure XIII.1: A classic Leyden jar where a voltage applied to the top electrode forces charges unto the strips. These charges repel each other, forcing the strips apart.

The advantage of this approach is that each longitude wire has the same length, and they can be folded together onto a spool for later unwinding and electrostatic inflation. This allows the density of the stored wires, especially if they were square instead of round, to approach the density of the constituent bulk material itself.

One of the key element of this architecture is the fact that the entire structure can be lifted in a single space shuttle launch. Assuming that each sphere is composed of a 1 mil diameter tungsten wire mesh with a 10 m pitch, the mass of the outer solar wind repelling sphere is 6,200 kg, while the middle deceleration sphere has a mass of roughly 1,550 kg. The inner containment sphere has a mass of a few hundred kilograms. Even with the addition of the assembly equipment, charging equipment, controls, diagnostics, and other miscellaneous hardware, the total mass is less than 10,000 kg. The shuttle is capable of lifting this mass to a 320 mile high circular orbit, even at orbital inclinations as high as 57º.

XIV. Delivery of the antimatter

Once the antimatter is cooled into antihydrogen snowflakes in the center of the harvester, the snowflakes can be slightly charged by either depleting or enriching the snowflake with positrons. A linear accelerator can then accelerate the snowflake out of the harvester toward a separate booster linear accelerator. This booster accelerator can increase the speed of the snowflake to that close to the speed of light.

Imagine space stations, lunar installations, asteroid habitats, and even accelerating space ships, receiving the antihydrogen snowflakes in a matching linear decelerator. Since quantities as small as milligrams will send spacecraft out of the solar system, very little energy is required to accelerate these snowflakes. This point-to-point delivery system would make delivery of antimatter around the solar system quite straightforward.

XV. Conclusions

This project was able to computationally evaluate the concept of antimatter harvesting, to develop a workable architecture that captures, cools, and delivers both antiprotons and positrons, and to address the construction issues of these harvesters.

This report was an architectural report describing the launch and deployment of antimatter harvesters; along with the capture, cooling, and antimatter delivery systems required to harvest antimatter in space and return it to Earth, or eventually to other destinations such as refueling depots in a solar system wide transportation network.